Biosensors and Bioelectronics 63 (2015) 525–532

Contents lists available at ScienceDirect

Biosensors and Bioelectronics

journal homepage: www.elsevier.com/locate/bios

Magneto-plasmonic biosensor with enhanced analytical response and stability

Sorin David [a], Cristina Polonschii [a], Catalin Luculescu [b], Mihaela Gheorghiu [a], Szilveszter Gáspár [a], Eugen Gheorghiu [a,c,*]

[a] International Centre of Biodynamics, Intrarea Portocalelor 1B, Bucharest 060101, Romania
[b] National Institute for Laser, Plasma and Radiation Physics, Atomistilor 409, Magurele 077125, Romania
[c] University of Bucharest, 4-12 Regina Elisabeta Blvd., Bucharest 030018, Romania

ARTICLE INFO

Article history:
Received 23 May 2014
Received in revised form
1 August 2014
Accepted 4 August 2014
Available online 8 August 2014

Keywords:
Magneto-optic surface plasmon resonance
Magnetic alloys
Surface plasmon resonance enhancement
Affinity biosensor
Angle-resolved surface plasmon resonance
Fixed-angle surface plasmon resonance

ABSTRACT

We present novel solutions to surpass current analytic limitations of Magneto-Optical Surface Plasmon Resonance (MOSPR) assays, concerning both the chip structure and the method for data analysis. The structure of the chip is modified to contain a thin layer of Co–Au alloy instead of successive layers of homogeneous metals, as currently used. This alloy presents improved plasmonic and magnetic properties, yet a structural stability similar to Au–SPR chips, allowing for bioaffinity assays in saline solutions. Analyzing the whole reflectivity curve at multiple angles of incidence instead of the reflectivity value at a single incidence angle provides a high signal-to-noise ratio suitable for detection of minute analyte concentrations. Based on assessment of solutions with known refractive indices as well as of a model biomolecular interaction (i.e. IgG–AntiIgG) we demonstrate that the proposed structure of the MOSPR sensing chip and the procedure of data analysis allows for long-time assessment in liquid media with increased sensitivity over standard SPR analyses.

1. Introduction

Surface Plasmon Resonance (SPR)-based methods are currently among the methods of choice to assess bioaffinity interactions at interfaces due to their sensitivity to local changes in the refractive index of adjacent media (Schasfoort and Tudos, 2008). Nevertheless, there is an unmet need to improve the sensitivity of the existing SPR assays. Possible avenues to gain more sensitivity include optimization of the multilayered sensor chip structure, improvement in the sensitivity of photodetectors (Schasfoort and Tudos, 2008) or signal modulation (Regatos et al., 2011; Sepúlveda et al., 2006). Some of the signal modulation approaches are based on the magneto-plasmonic effects (Armelles and González-Díaz, 2008; Belotelov et al., 2013; Temnov et al., 2010). This is accomplished by employing the transverse magneto-optic Kerr effect (TMOKE). The TMOKE effect occurs as a result of applying a magnetic field perpendicular to the propagation plane of the incident p-polarized light and in the plane of a film with magneto-optical properties determining changes in the intensity of the reflected light (Zvezdin and Kotov, 1997). The combination of TMOKE with plasmonic effects (Raether, 1988) lays the foundation of a novel SPR detection configurations, i.e. the magneto-optical SPR (MOSPR) technique (Armelles et al., 2013). Modulation of the reflectivity (i.e. SPR) curve is accomplished by applying an alternative transversal magnetic field, perpendicular to the propagation plane of an incident p-polarized beam of light (Zvezdin and Kotov, 1997), onto a sensor chip exhibiting both magnetic and plasmonic properties (Sepúlveda et al., 2006). When the plasmons are excited, one notices a MOSPR response presenting increased sensitivity to the refractive index changes. This approach yields a reported theoretical improvement in the sensitivity of sensing assays of one (Regatos et al., 2010; Sepúlveda et al., 2006) or even two (Pištora et al., 2010) orders of magnitude.

Usually, the chips for magneto-plasmonic applications comprise metallic multilayers or nanostructures (e.g. nanodiscs, nanocrystals) (Armelles and González-Díaz, 2008; Belotelov et al., 2013; Temnov et al., 2010), whose fabrication could be technologically challenging. For sensing, current MOSPR assays employ multilayered structures; however, these complex structures exhibit lack of stability when exposed to or interrogating (saline) liquid samples. Therefore they are mostly used as gas sensors due to their increased sensitivity as compared to classical SPR assays (Armelles et al., 2013; Manera et al., 2012, 2011). The poor stability in liquids can be due to magnetostrictive effect (Regatos et al.,

* Correspondence to: International Centre of Biodynamics, Intrarea Portocalelor 1B, 060101 Bucharest, Romania. Tel.: +40 21 3104354; fax: +40 21 3104361.
E-mail address: egheorghiu@biodyn.ro (E. Gheorghiu).

http://dx.doi.org/10.1016/j.bios.2014.08.004
0956-5663/

2011), which is the more pronounced, the more heterogeneous the layers in the sensor structure.

We developed and tested a multilayered chip comprising a thin film of amorphous Au–Co alloy, capped with a layer of Au (to allow further functionalization), exhibiting both plasmonic and magnetic properties, and increased stability in (saline) liquid media.

Optimized raw data analysis provides additional routes for sensitivity enhancement. Therefore, both angle-resolved SPR/MOSPR curves (i.e. the entire angular range of the SPR curve) or the reflectivity values at a single (fixed) angle of incidence, the latter being employed in most current SPR/MOSPR assays (Manera et al., 2012), have been comparatively evaluated.

We demonstrate that the proposed *angle-resolved* MOSPR bioassay based on a Co–Au alloy thin film exhibits both increased sensitivity in comparison with the current SPR/ MOSPR approaches and high stability (similar to the one achieved with classic, gold-only, SPR chips) even when addressing saline liquid samples.

2. Material and methods

2.1. Materials

Bovine serum albumin (BSA), human IgG (HIgG), affinity-isolated anti-human IgG (AHIgG), N-hydroxysuccinimide (NHS), 1-ethyl-3-(dimethylaminopropyl) carbodiimide (EDC) and ethanolamine were purchased from Sigma-Aldrich (Germany). (11-Mercaptoundecyl)hexa(ethylene glycol) acetic acid was purchased from Prochimia Surfaces, Poland. Surfactant P20 was provided by GE Healthcare. Au pellets (99.999%), Co (99.99%) pellets and Ti sputter target (grade 2) were purchased from Kurt J. Lesker USA. N-BK7 glass wafers were purchased from Sydor Optics UK. All the other reagents for buffers were purchased from Sigma.

The buffers used for the experiments are: immobilization buffer, 10 mM acetate buffer pH 5; running buffer: HBS-EP buffer (10 mM HEPES pH 7.4, 150 mM NaCl, 3 mM EDTA, and 0.005% Surfactant P20).

Ultrapure water (Millipore) was used throughout the preparations. All chemical reagents were of analytical grade and were used without further purification.

2.2. Fabrication of SPR and MOSPR chips

Substrates of BK7 glass (0.3 mm × 4 mm × 11 mm) are cleaned by successive sonication in water, acetone and isopropanol and dried in a stream of nitrogen. Further, the substrates are exposed to oxygen plasma and heated to 150 °C for degassing. The pressure inside the evaporation chamber was kept to approximately 2×10^{-6} Torr. Samples were rotated at 10 rot min^{-1} to ensure uniform coating. All the deposition processes were done at room temperature. The thickness of the deposited layers is constantly monitored by a quartz crystal microbalance inside the evaporation chamber. A layer of Ti (4 nm) is first sputtered on the glass substrates for improving the adhesion of subsequent layers. All metals are deposited by thermal evaporation, with the exception of Ti which is sputtered (RF sputtering at 5×10^{-3} Torr Ar pressure and 8 W cm^{-2}). The Au and Co layers are thermally evaporated at rates of 0.5 Å s^{-1} and 3 Å s^{-1} respectively.

Standard SPR chips are fabricated by evaporating 50 nm of Au onto the Ti-modified substrates.

The Au–Co–Au tri-layer consists of a 26 nm Au, 6 nm Co layer, separated from the sensing surface by a 12 nm Au layer. An intermediate layer of 2 nm Ti is inserted between Au and Co to improve adhesion of the two metals.

2.3. The alloy based magneto-plasmonic sensor chip

Currently, different metallic alloys are used for enhancing the plasmonic response (Blaber et al., 2010). Applications of Au–Co composites are mostly related to jewelry to harden the gold and in microelectronic industry as coatings for wear resistant electrical contacts (Goodman, 2002; Okinaka, 1998). Since alloys containing more than ~1% cobalt also exhibit magnetic properties (Kahn, 1992), the Au–Co thin films feature enhanced magneto-plasmonic behavior (Yang et al., 2010).

An important step in the preparation of the sensor chip is the deposition of the composing metal layers. Several techniques have been reported as suitable options for deposition of alloys each with their advantages and pitfalls. Pressure Vapor Deposition (PVD) using the sputtering technique has been used for depositing alloys (Kahn, 1992; Mattox, 2010; Yang et al., 2010); however magnetron sputtering of magnetic materials requires expensive magnetron guns with powerful magnets. Moreover, manufacturing custom sputtering targets comprising gold alloys may have prohibitively high costs. E-beam epitaxy may be also used for growing crystalline films with well controlled magnetic properties, but this is suitable or limited to substrates with crystalline structure (Ferreiro-Vila et al., 2011). Aiming for a simple and cost-effective deposition procedure, we chose the thermal evaporation method in which the metals to form the alloy are mixed and melted from a single source. Despite the different melting points (i.e gold – 1064 °C and cobalt – 1495 °C), the temperatures for reaching a given vapor pressure are similar for the two materials (gold – 947 °C and cobalt – 990 °C for a vapor pressure of 10^{-6} Torr) (Mattox, 2010). Therefore, both metals reach similar evaporation rates at a vacuum pressure of 10^{-6} Torr (Mattox, 2010), the deposited film having a slight depletion of cobalt compared to the composition in the source (as revealed by composition analysis).

The proportion of Au and Co in the alloy should allow for both good plasmonic properties and elevated magnetic characteristics. If there is too much of cobalt in the alloy, there will be an inconvenient dampening in the SPR effect exhibited by gold; conversely, too less cobalt would trigger a limited magnetic effect. Therefore, we have selected an alloy with a volumetric proportion of 10% Co:90% Au, a ratio also providing a good miscibility of the melted substrates (Okamoto et al., 1985) as well as magneto-plasmonic behavior (Yang et al., 2010). A higher proportion of cobalt in the alloy was tested but resulted in a poor SPR signal (data not shown).

Au–Co thin films form nanocomposites comprising clusters of Au and Co with sizes directly proportional to the temperature of the substrates during deposition (Yang et al., 2010). Accordingly, we chose to deposit a thin film of Au–Co alloy at room temperature. Despite yielding a lower magneto-optic (MO) effect, the film obtained under these conditions presents Co clusters of small size (~150 nm) (Yang et al., 2010), potentially leading to smaller magnetostriction and increased stability of the MOSPR chips.

According to Yang et al., the Au–Co mixture, deposited (by sputtering) in thin films, has in-plane anisotropy of the magnetization and a magnetic moment correlated with the amount of Co present. In several studies (e.g. He and McGahan, 1991; Kockar and Meydan, 2002) magnetron-sputtered films and evaporated films of composited materials present similar magneto-optical properties. Hence, we consider that our Co–Au alloy film presents also in-plane anisotropy similar to the Co–Au composite films obtained by magnetron sputtering co-deposition.

The Au–Co alloy chips are fabricated by evaporating a 30 nm layer of Au–Co alloy followed by 15 nm of Au. No intermediate Ti layer is used. The alloy is thermally evaporated at a rate of 0.5 Å/s from a single tungsten boat containing corresponding quantities of

Au and Co to yield an alloy of 10% co-volumetric ratio (588 mg Au and 27 mg Co). Scanning Electron Microscopy Energy-Dispersive X-ray spectroscopy (SEM-EDX) measurements are performed to verify the composition of the evaporated alloy films (before capping with the Au layer). The measurements have been done in a scanning electron microscope (FEI Co., model Inspect S) with an Si(Li) energy dispersive detecting unit (EDAX Inc., EDAX, model ECON 4/6) operated at an electron beam voltage of 20 kV. Every spectrum was acquired at 1000× magnification from an area of approximately $250 \times 250\ \mu m^2$. Results show a ratio of 8 atoms of Au to 1 atom of Co, corresponding to a volumetric ratio Au:Co of 9.2:0.8.

2.4. Chip functionalization and bioaffinity assays

(MO)SPR chips are functionalized by immersion in an ethanol solution containing 1 mM of 11-PEG–COOH thiol for 3 h. Functionalized chips are mounted in the flow chamber of the measurement setup and further modified with the ligand (HIgG) by amine coupling (Johnsson et al., 1991). For this coupling, first a mixture of 100 mM NHS and 400 mM EDC is passed over the chip for 7 min to activate the carboxylic groups of the thiol. Then, the ligand (30 μg/ml) is injected for 30 min in a 10 mM acetate buffer at pH 5.5 to promote electrostatic pre-concentration. The so-modified surface is deactivated for 7 min with 1 M ethanolamine (pH 8.6) and finally blocked and tested for nonspecific adsorption by injecting a solution of 1 mg/ml BSA in HBS (10 min). The entire immobilization procedure is performed at a flow rate of 30 μl/min. The running buffer for the ligand immobilization is HBS.

The bioaffinity assay is performed at 100 μl/min, by injecting successively different concentrations of the analyte (A-HIgG) in the range 5–80 nM in HBS (2 min). Sequential injections of increasing concentrations of AHIgG, without the regeneration steps, are performed (Karlsson et al., 2006). The analyte of smallest concentration is first injected for 2 min. Then the surface is washed with buffer for another 2 min and the next concentration of analyte is injected. The cycle is repeated for all concentrations and when the series is completed, the surface is regenerated with two pulses of glycine 10 mM pH 2 (2 × 2 min).

2.5. SPR/MOSPR measurements

Fig. 1 outlines the MOSPR concept (see Supplementary data for details). In brief, the measurement setup, described in more detail elsewhere (David and Gheorghiu, 2011), comprises an SPR module and an external electromagnet for applying the alternating transverse magnetic field, in a Flow Injection Analysis (FIA) setup. The SPR measurement module is based on a SPREETA sensor model TSPR1K23 (Texas Instruments USA) with customized fluidics and a data acquisition board that gives online access to curve measurements. In the SPR module with Kretschmann configuration (Raether, 1988), the backside of the chip is illuminated using a divergent p-polarized beam of light that provides a continuous range of incidence angles, spanning the angular domain, 62–73°. The reflected light is assessed by a linear photodetector array comprising 128 pixels, each pixel measuring the intensity of the reflected light corresponding to a different angle of incidence. This allows for virtually simultaneous acquisition of reflectivity data, the whole SPR curve being measured in ~5 ms. The wavelength used is in the near infra-red region of the spectrum (840 nm) and provides a rather sharp dip and large penetration depths for standard SPR measurements of Au chips in aqueous media. The relation between the individual pixels of the photo detector array and the corresponding angle of incidence is derived using the manufacturing parameters of the sensor. Calibration measurements involve injections of water and glycerol solutions of various concentrations of known refractive index. Calibration curves are established linking the variations of the measured SPR angle to refractive index modification. SPR measurements are expressed as refractive index variations versus time (i.e. sensorgrams) or concentrations of analyte (i.e. calibration curves). The gold layer of the SPREETA sensor is removed using aqua regia (Neuert et al., 2005). Tailored sensor chips are placed on the cleaned glass window of the SPREETA using oil of matching refractive index.

MOSPR measurements are performed while actuating the incorporated transversal electromagnet with a sinusoidal voltage. A current of 120 mA is required for yielding field strengths of up to 5 mT (demonstrated sufficient for saturation of the magneto-optical chips).

Applying the alternative magnetic field did not create significant heating of the electromagnet nor did it have an effect over the SPR measurement on a classical gold surface, proving that there is no crosstalk between the magnetic field and the electronic and optic components of the SPREETA chip.

3. Results and discussion

3.1. Characterization of (MO)SPR chips

The thickness of the magneto-plasmonic layer was chosen based on simulations using the refractive index values corresponding to 840 nm, the wavelength of the SPR module, as revealed from Fig. 2A. Layer thickness, and its position within chip structure were varied to obtain a sharp SPR curve fostering similar features as the one exhibited by the classical SPR 50 nm gold layer. The 15 nm gold capping layer was employed to ensure uniform and complete coverage of the magneto-plasmonic layer. The SPR curves of the proposed structures were simulated using the transfer matrix approach (Olaru et al., 2009) based on reference optical constants (Polyanskiy, 2014) (for each metal and layer thickness). In Fig. 2A we present the theoretical SPR curves for the standard 50 nm Au layer, the Au–Co–Au tri-layer and the Au–Co alloy film. For the Au–Co alloy the optical constants were derived based on Lorentz–Lorenz relation (also tested via a generalized transfer matrix approach). From the simulation it is evident that the curve for the Au–Co alloy presents a dip in the same angular region as the curve for Au and a less dampening effect as of the

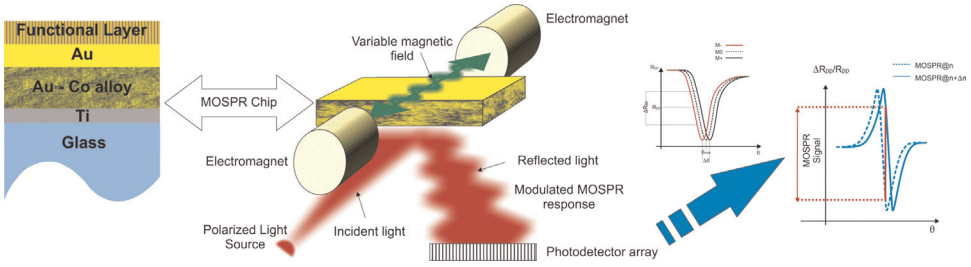

Fig. 1. The magneto-optical SPR concept.

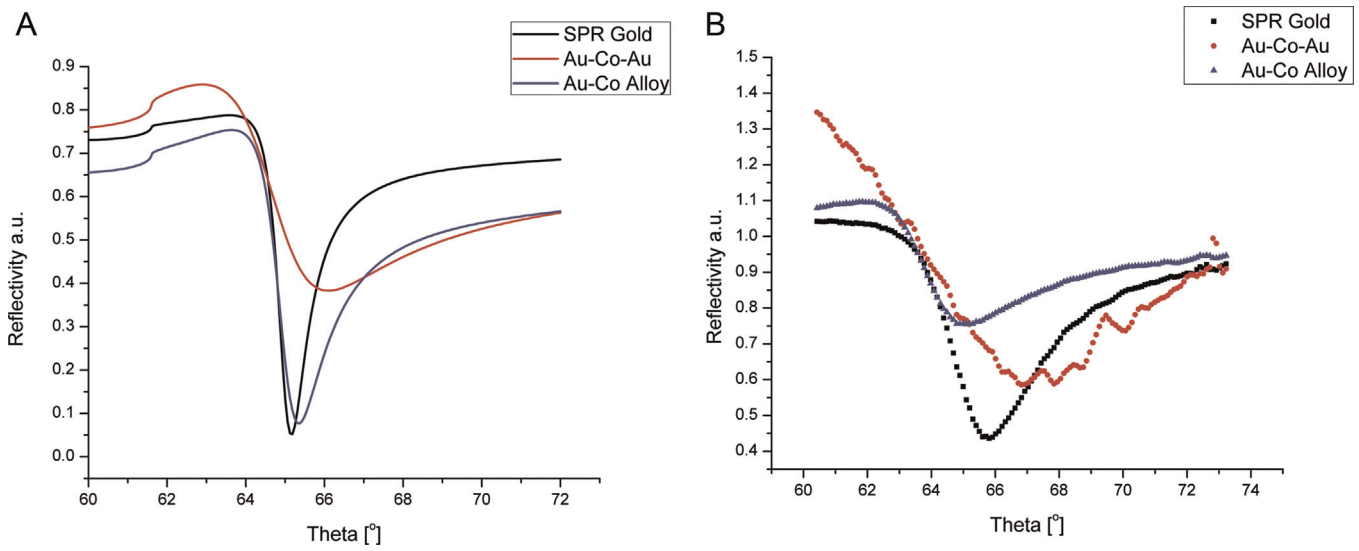

Fig. 2. (A) Theoretical SPR curves for 50 nm Au (black), Au–Co–Au trilayer (red) and Au–Co alloy (blue). (B) Experimental SPR curves for 50 nm Au (black), Au–Co–Au trilayer (red) and Au–Co alloy (blue). (For interpretation of the references to color in this figure legend, the reader is referred to the web version of this article.)

Au–Co–Au tri-layer structure (Fig. 2A). The MOSPR signal is derived from the SPR curves at different magnetization states of the sensor chip (two alternative methods described in Supplementary data).

The experimental SPR curves for the three types of chips are shown in Fig. 2B. The difference in width, depth and SPR dip position of the measured over theoretical data originates from the documented modification of the optical constants of thin layers due to the roughness of the films (Liu et al., 2010). The roughness introduces a supplementary parameter in the k_{spp} wave vector leading to alteration of the shape of the SPR curve (Fontana and Pantell, 1988; Kolomenski et al., 2009) with respect to the theoretical simulations. There is also an effect of damping due to the presence of the Co material that yields a shift in the resonance values and a less sharp dip for the alloy and the tri-layer (Ghatak, 2010) structures.

Resonance curves are characterized by the Q factor – a dimensionless parameter defining the sharpness of the dip-calculated as the ratio between the width at half height and the position of the minimum of reflectivity. The higher the Q-factor, the narrower and sharper the curves are. To numerically quantify the shape of the SPR curves, a similar treatment as the one performed on the resonance curves is considered. The Q-factor was previously used to characterize SPR curves (Beheiry et al., 2010; Hu et al., 2009; Le and Bienstman, 2011; Ma et al., 2014). A high Q-factor leads to sharp resonant peaks that allow better detection of the minima and higher variation pertaining to single angle measurements (as a function of the refractive index changes), hence to improved SPR sensitivity. The Q-factor is used to compare the 3 type of sensors in terms of SPR dip shape and its related effects on SPR sensitivity. We calculated the relative Q factors for theoretical and experimental SPR curves of MOSPR chips versus the respective Q factors of a classic SPR Au chip and we obtained a value of 61.8% for the Au–Co alloy and a value of 31% for the Au–Co–Au trilayer for the theoretical curves. In the cases of the experimental curves the values were 78.2% and 48.2% respectively. Both theoretical and experimental data show that the Q factor for the Au–Co alloy is higher than in the case of the tri-layer; however, it is lower with respect to gold.

The magneto-plasmonic behavior of MOSPR chips is analyzed while applying a sinusoidal magnetic field (5 mT amplitude of the alternating magnetic field strength, 0.3 Hz frequency). These conditions were determined by applying alternating magnetic fields of various strengths (data not shown). A field strength of 5 mT was used throughout the MOSPR experiments as larger fields did not provide higher MOSPR signals.

Oscillations exhibited by the reflectivity measured by the detector in the case of a MOSPR chip reveal the magneto-optical response of the chip (Fig. 3A). The reflectivity oscillates as the magnetization states of the, initially non-magnetized, MOSPR chip are changing in response to the application of an alternating transversal magnetic field. There is no magneto-optical effect on a standard, Au SPR sensor chip and also no effect of the alternating magnetic field on the electronic components of the SPR module (data not shown).

Hysteresis TMOKE loops are recorded for the Au–Co–Au tri-layer and the Au–Co alloy to further investigate the magneto-optic effect present in these structures (Fig. 3B). The loops, showing changes in the relative magnetization in response to the intensity of the applied magnetic field, demonstrate the magneto-optic activity of both structures.

The stability of the MOSPR chips in physiological solutions is tested by exposure to a saline solution (e.g. HEPES buffer solution – HBS) while applying the oscillatory magnetic field. Time series SPR measurements are performed to assess the stability of the sensing surface of the MOSPR chips. The initial baseline is recorded in water (ultrapure water n@840 nm = 1.32757) (Polyanskiy, 2014) and then the HBS solution is injected. The refractive index derived from SPR curve is plotted over time. While the alloy shows no sign of destabilization (for virtually indefinite exposure, similar to regular Au sensor chips), in the case of the Au–Co–Au tri-layer there is a significant and rapid drop in the signal caused by exfoliation of the metallic film (Fig. 4 and its inset). Increase in the transparency of the film (observed under transmission microscopy, Fig. 4 inset) further amplified with longer exposure lead us to the conclusion that the film is indeed exfoliating. Under the same flow conditions and buffers composition no modifications (i.e. salt deposition) were observed in the cases of plain gold (data not shown) and/or Au–Co alloy (transmission microscopy-data, not shown).

A further confirmation of the stability of the Au–Co alloy chip when exposed to saline solutions is given by recovery of the same response (the initial baseline level) when returning to water (Fig. 4 black line). The stability of the Au–Co alloy is further tested in the functionalization and immobilization steps in which the sensing

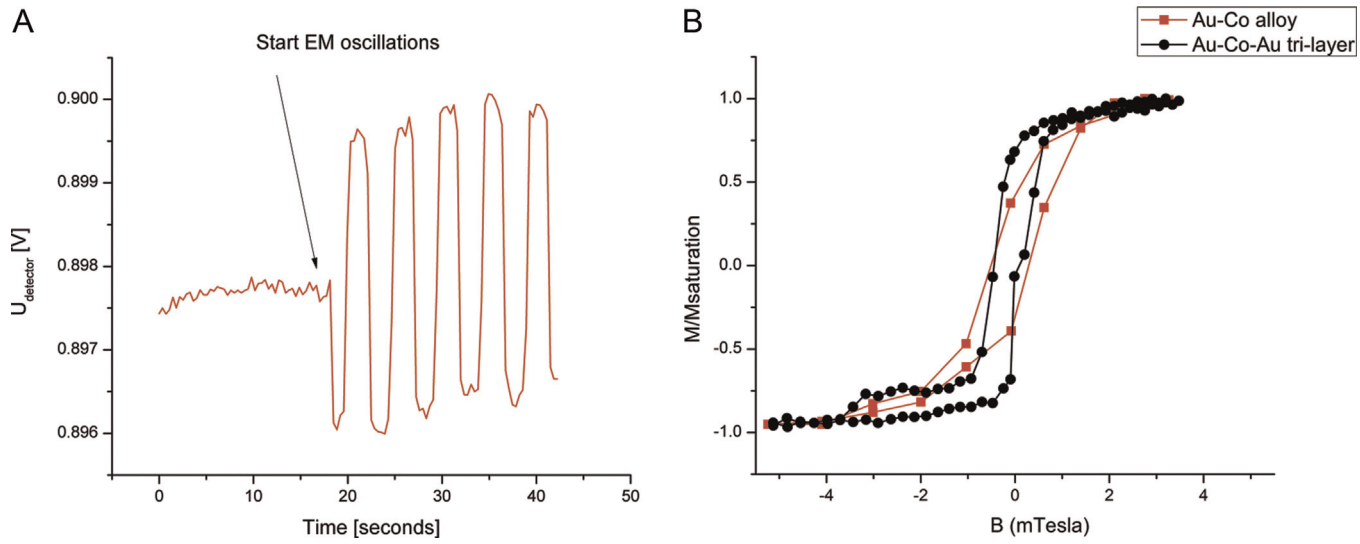

Fig. 3. (A) Oscillations in the reflectivity of an Au–Co–Au tri-layer MOSPR chip as measured on the photodetector (recalculated data from fitted SPR curve – details in Supplementary data). (B) TMOKE loops for Au–Co alloy (black) and Au–Co–Au tri-layer (red) – the relative magnetization (normalized to maximum value $-M_{saturation}$) as a function of the applied magnetic field strength. (For interpretation of the references to color in this figure legend, the reader is referred to the web version of this article.)

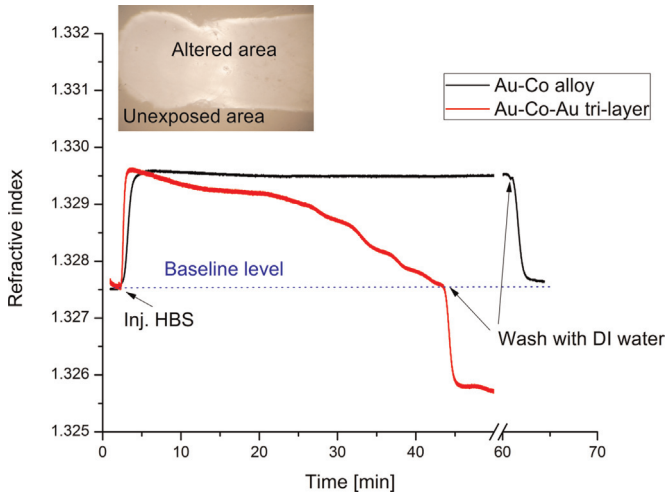

Fig. 4. Stability measurements for Au–Co alloy (black) and Au–Co–Au tri-layer (red) at injection and continuous flow of HBS solution in oscillatory magnetic field. Inset – Optical image of an Au–Co–Au tri-layer chip showing pronounced corrosion in the areas exposed to saline solution whilst no corrosion is evident in areas protected from this solution. (For interpretation of the references to color in this figure legend, the reader is referred to the web version of this article.)

surface is prepared for antibody–antigen interactions. No damage to the Au–Co alloy chip was observed during these steps.

3.2. (MO)SPR measurements and data processing

For classical SPR measurements, the response is derived from the SPR curve (i.e. reflectivity values as function of the incidence angle) as the variation of the angle for which the minimum of the reflectivity is recorded (Schasfoort and Tudos, 2008). This angle, called the SPR angle (θ_{min}), depends on the refractive index of the media in the immediate vicinity of the sensing surface (Schasfoort and Tudos, 2008) and is determined most precisely if the reflectivity dip is the sharpest. Changes at the sensing surface, accompanied by a modification of the refractive index, cause a shift in the SPR angle that is used for label free assessment of biomolecular surface interactions. This is the preferred mode of operation for real-time measurements having a linear dependence on the refractive index changes and the amount of molecules accumulated on the surface (Schasfoort and Tudos, 2008). Various analytical methods were developed to improve sensitivity, robustness against noise (Chinowsky et al., 1999) and time of analysis (Zhan et al., 2011) and are based on the same full curve analysis.

In the case of MOSPR, for (bio)sensing assays, one has to process the MOSPR curves and derive the analytic signal versus the quantity of analyte to be detected. Reflectivity data for the entire angular range (SPR curves) are collected and fitted with a rational polynomial equation (see Supplementary data for details, fitting function of SPR data). The fitted SPR curves provide corrected reflectivity values for each incident angle and are used to calculate the MOSPR curves (Fig. S3D). These smoother MOSPR curve are used for further processing.

The MOSPR response is derived either

a. based on the SPR angle (θ_{min}) (Ferreiro-Vila et al., 2009; González-Díaz et al., 2007)

$$\frac{\Delta k_{SPP}}{k_{SPP}} = \cot(\theta_{min})\Delta\theta \quad (1)$$

where k_{SPP} is the wavevector for the surface plasmon polaritons under conditions of no magnetization and Δk_{SPP} is the variation of the wavevector in response to the alternating magnetic field $\Delta k_{SPP} = k_{SPP}(+M) - k_{SPP}(-M)$, θ_{min} is the SPR angle and $\Delta\theta$ is the angular shift due to magnetic field modulation,

or,

b. From the reflectivity values corresponding to a selected Angle of incidence, as the variation of the reflectivity R_{pp} while switching the direction of the *in plane* magnetization of the sensor (Armelles et al., 2013)

$$\frac{\Delta R_{pp}(\theta)}{R_{pp}(\theta, 0)} = \frac{R_{pp}(\theta, +M) - R_{pp}(\theta, -M)}{R_{pp}(\theta, 0)} \quad (2)$$

where $R_{pp}(\theta,+\mathrm{M})$ and $R_{pp}(\theta,-M)$ represent the reflectivity values at a certain incidence angle for the direction of the *in plane* magnetization perpendicular to the propagation plane of the incident p-polarized light in both directions and $R_{pp}(\theta,0)$ represents the reflectivity without magnetization at the same angle. In

real measurements, $\Delta R_{pp}(\theta)$ is obtained from the amplitude of the oscillations of the measured reflectivity (Fig. 3A) upon application of the alternating magnetic field. The MOSPR curve shown in S3F is defined as the variation of the $\Delta R_{pp}\Delta R_{pp}(\theta)/R_{pp}(\theta)$ ratio versus the angle of incidence of the light.

3.3. Sensitivity comparison of MOSPR and SPR sensors

Thus, to characterize the new MOSPR chips, we investigate the differences between SPR/MOSPR responses in terms of sensitivity and signal-to-noise ratio when analyzing: (a) the full SPR curve and (b) the reflectivity at a given, single angle of incidence.

a) When considering signal analysis based on the SPR angle (Eq. (1)), derived from the fitted curve (see Supplementary data – fitting function of SPR data) on MOSPR data, the Fourier analysis provides the amplitude (corresponding to $\Delta\theta$) and mean value (corresponding to θ_{min}) when applying an oscillating magnetic field. Consequently, using Eq. (1) one obtains the MOSPR response. In Fig. 5A, we plotted the SPR and MOSPR responses when measuring solutions with known refractive indices (i.e., ultrapure water and 1%, 2%, 3% and 5% glycerol solutions, having refractive indices of 1.32757, 1.32858, 1.32925, 1.33108, and 1.33358, respectively, for the 840 nm wavelength) with sensor chips comprising Au (classical SPR), Au–Co alloy and Au–Co–Au tri-layer (for MOSPR). Notably, the Au–Co–Au tri-layer is only stable in ultrapure water and aqueous solutions of glycerol. The relative response for the SPR and MOSPR is calculated as $(V_i - V_0)/V_0$, where V_i is the current value of the MOSPR/SPR response and V_0 is the value recorded at the smallest concentration.

Fig. 5A outlines the predicted sensitivity improvement of the MOSPR assay comprising the alloy chip in comparison with classical SPR on Au and MOSPR on Au–Co–Au tri-layer (almost 4 times increase).

However due to the limited *Q*-factor of the SPR curves exhibited by magneto-plasmonic chips, the actual MOSPR signal presents a lower signal to noise ratio (SNR) as compared to the

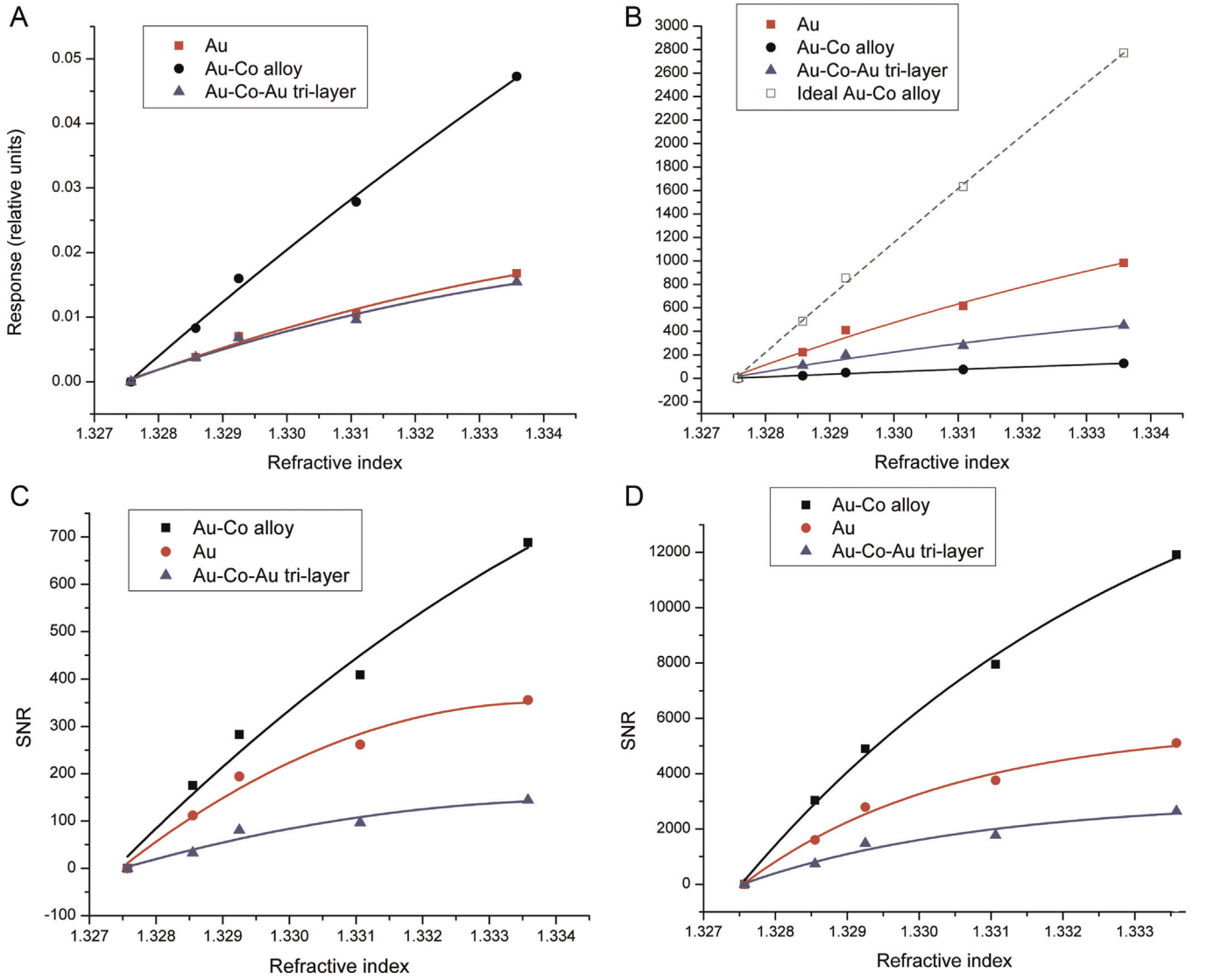

Fig. 5. (A) SPR signals recorded with Au chip (red) compared to MOSPR signals recorded with either the tri-layer structure (blue) or the alloy (black) for solutions having different refractive indices; (B) signal to noise ratio as function of refractive index and chip structure (Au – red, tri-layer – blue, alloy – black); the signal to noise ratio of an idealized alloy MOSPR chip (green) is given as reference for the targeted sensitivity after experimental set-up optimization. (C) The evolution of signal to noise ratio for Au–SPR (red), Au–Co alloy–MOSPR (black) and Au–Co–Au tri-layer–MOSPR (blue) at different refractive indices – raw reflectivity data. (D) The evolution of signal to noise ratio for Au–SPR (red), Au–Co alloy–OSPR (black) and Au–Co–Au tri-layer–MOSPR (blue) at different refractive indices – reflectivity values derived from fitted SPR curves. (For interpretation of the references to color in this figure legend, the reader is referred to the web version of this article.)

ideal values (Fig. 5B). The SNR is defined as the ratio between the response (SPR, MOSPR) and the corresponding root mean square deviation (RMSD, calculated on 100 data points). Thus, in spite of the increased Δk_{SPP} signal of the MOSPR chips, defined in Eq. (1), due to the limited precision to determine the magnitude of the angle shift, $\Delta\theta$, there is no improvement of the SNR (Fig. 5B). Ideally, by combining the plasmonic behavior of gold (sharp dip, large *Q*-factor) with the magneto-optical features of the tri-layer, the most sensitive MOSPR signal would be obtained (Fig. 5B, ideal Au–Co alloy). Notably the ideal MOSPR response presented in Fig. 5B would be provided by a chip able to feature both an SPR curve with the *Q* factor of the classic SPR Au chip and the MO response of the Au–Co–Au tri-layer chip. Hence, the ideal MOSPR response is derived based on real data measured on a classic SPR Au chip (that provides the θ_{min} values) and a Au–Co–Au tri-layer with MO response (corresponding to $\Delta\theta$) by applying Eq. (1). Accordingly, one can predict that MOSPR sensitivity may be even greater if smoother surfaces with sharper SPR dips are obtained. Such an approach will also have the benefit of a linear dependence of the signal over the local refractive index changes, and subsequently on the amount of the adsorbed analytes (e.g., proteins) (Lofas, 1995; Schasfoort and Tudos, 2008). In short, Fig. 5A shows the MOSPR and SPR signals without normalization versus the noise (i.e. RMSD); in contrast, Fig. 5B presents the SNR of the MOSPR and SPR curves (ratio between the response and the RMSD).

b) According to Eq. (2), the MOSPR signal is derived from $\Delta R_{pp}(\theta)/R_{pp}(\theta)$ data using the value of the reflectivity corresponding to a selected angle of incidence θ_s, chosen to yield the highest sensitivity. At this angle, the MOSPR curve (i.e. $\Delta R_{pp}/R_{pp}$ vs. incidence angle) presents the steepest slope (Armelles et al., 2013). We derive the θ_s angle by analyzing the derivative of the fitted SPR curve. Time series of full curves are recorded, then fitted and the reflectivity values (corresponding to θ_s) plotted over time (Fig. S3C). Further, frequency (Fourier) analysis is performed to extract the amplitude of oscillations (corresponding to ΔR_{pp}) and their mean (corresponding to R_{pp}). MOSPR and SPR reflectivity responses derived from raw measurements directly from the detector corresponding to θ_s are presented in Fig. 5C, while reflectivity responses calculated from fitted SPR curves are given in Fig. 5D. The comparison shows that fitting the curves (and hence reducing the noise) improves the sensitivity greatly (Fig. 5D). The sensitivity increase for the Au–Co alloy chip with respect to gold is 1.5 fold for the raw reflectivity approach and reaches 2.5 times when using the reflectivity values derived from fitted SPR curves. In summary, Fig. 5C and D compare the SNR curves derived: (1) directly from the raw reflectivity data and (2) when using the fitted SPR data. This highlights the advantage of our method in terms of improving on the SNR for both SPR and MOSPR assays.

3.4. Bioaffinity assay

To test the efficiency of the developed approach, both the advanced transducer, and method for data analysis, in assessing bioaffinity binding, a model antigen–antibody interaction, were used. Affinity tests, using the model biomolecular interaction between human immuno-globulin G (HIgG) and Anti-HIgG in a direct assay (Schasfoort and Tudos, 2008), were performed.

In the following, MOSPR assays of bioaffinity interactions are shown only for alloys. Because of the corrosive effect of the saline buffers, the Au–Co–Au tri-layers cannot be used even after surface modification and functionalization.

The sensor chip surfaces of both the Au–Co alloy and Au were first functionalized using a carboxylated thiol and then further modified with HIgG via an amine coupling reaction. Several concentrations of Anti-HIgG (ranging from 5 to 80 nM) were injected consecutively over the sensor′s surface and the response was recorded (Fig. 6A). As one can observe, the MOSPR signal shows good stability during the experiment: after regeneration (when the bioaffinity complexes are broken up and Anti-HIgG washed away) the signal always returns to initial baseline values, and comparable signals (CV of 6.9%) are obtained for five rounds of affinity binding (only two shown in Fig. 6A).

The improvement of the SNR for the Au–Co alloy based MOSPR assay as compared to the Au-based classic SPR assays (Fig. 6B) is evaluated by comparing the limit of detection (calculated as 3 times the standard deviation of blank), which is around 0.60 nM for the MOSPR assay and 0.96 nM for the SPR assay, an improvement of 160% of the sensitivity of MOSPR over SPR assays. The full calibration curves are presented in Fig. S4.

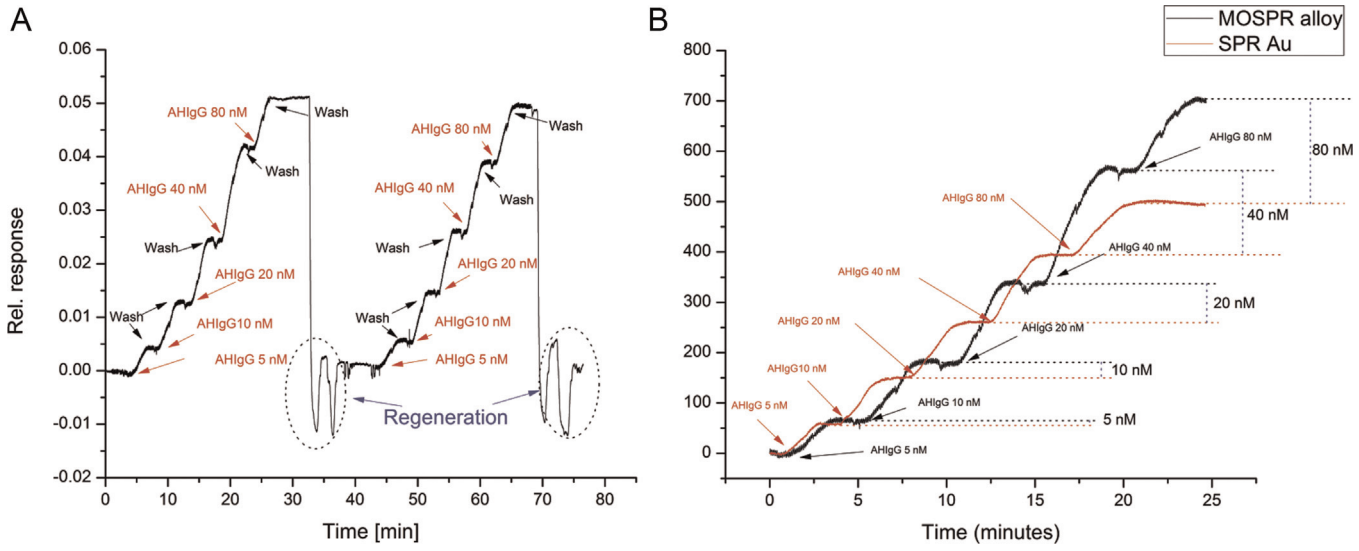

Fig. 6. (A) Relative response for several specific injections of Anti-HIgG (concentration range 5–80 nM) and two regeneration steps on the MOSPR Au–Co alloy chip (MOSPR detection). (B) Specific MOSPR (for Au–Co alloy – black) and SPR (for Au chip – red) responses for several injections of Anti-HIgG. The difference between washing levels for each concentration in the two cases (MOSPR and SPR) are marked with dotted lines. (For interpretation of the references to color in this figure legend, the reader is referred to the web version of this article.)

The intrinsic high noise of the detector within this proof-of-concept detection system used has so far limited the quantitative gain in sensitivity to approximately 2 fold for the small variations related to antigen–antibody interactions in the concentration range of 0–80 nM. Nevertheless, the sensitivity and stability of the proposed solution warrants wider applicability of magneto-plasmonic alloys in (bio)sensing assays and is equally applicable to other detection schemes such as the ones based on a lock-in amplifier. Added bonuses of digital processing of the measured signal, as proposed in our study, involve reduced costs and, having in mind the computing power of current processors, the fact that they can be also performed online.

4. Conclusions

A magneto-plasmonic sensor chip with a novel structure, comprising a thin film of 30 nm Au–Co alloy, capped by a 15 nm Au layer was manufactured and tested showing both a higher sensitivity than classic SPR, performed on a 50 nm thick Au film and excellent physical chemical and biochemical stability suited for biosensing applications in common buffers. We demonstrate a higher sensitivity featured by the MOSPR sensor based on the Au–Co alloy with respect to classical SPR when using the entire angular SPR range for full SPR curve analysis instead of classical fixed angle measurements. Notably, the proposed full SPR curve analysis enhances the sensitivity of both SPR and MOSPR assays. Although the relatively high intrinsic noise of our photodetector (SPREETA sensor) limits the quantitative gain in sensitivity to approximately 2 fold for the small variations related to antigen–antibody interactions in the concentration range of 0–80 nM, the sensitivity and stability of the proposed solution warrant wider applicability of magneto-plasmonic alloys in (bio)sensing assays. Full curve analysis allowed us to detect the minute angular changes of the reflectivity due to the TMOKE effect. Further improvements in detector sensitivity and/or application of a lock-in detection scheme may reduce the noise components and provide an even better SNR at low analyte concentrations. The proposed calculation method can nevertheless be employed regardless of the preferred frequency analysis method. Moreover, modifications in the structure and roughness of the chip to deepen the SPR dip and reduce its width may further improve the precision and sensitivity of MOSPR assays.

Acknowledgement

The authors thank the Romanian Executive Unit for Higher Education, Research, Development and Innovation Funding for funding through Grants PN II-ID-PCCE-2011-2-0075 and PN-II-RU-PD-2012-3-0467.

Appendix A. Supplementary data

Supplementary data associated with this article can be found in the online version at http://dx.doi.org/10.1016/j.bios.2014.08.004.

References

Armelles, G., Cebollada, A., García-Martín, A., González, M.U., 2013. Adv. Opt. Mater. 1, 10–35. http://dx.doi.org/10.1002/adom.201200011.
Armelles, G., González-Díaz, J., 2008. Opt. Express 16, 3112–3114.
Beheiry, M., El, Liu, V., Fan, S., Levi, O., 2010. Opt. Express 18, 22702–22714.
Belotelov, V.I., Kreilkamp, L.E., Akimov, I.A, Kalish, A.N., Bykov, D.A, Kasture, S., Yallapragada, V.J., Venu Gopal, A., Grishin, A.M., Khartsev, S.I., Nur-E-Alam, M., Vasiliev, M., Doskolovich, L.L., Yakovlev, D.R., Alameh, K., Zvezdin, A.K., Bayer, M., 2013. Nat. Commun. 4, 2128. http://dx.doi.org/10.1038/ncomms3128.
Blaber, M., Arnold, M., Ford, M., 2010. J. Phys. Condens. Matter 22, 143201.
Chinowsky, T.M., Jung, L.S., Yee, S.S., 1999. Sens. Actuators B Chem. 54, 89–97.
David, S., Gheorghiu, E., 2010. Towards an advanced magneto-plasmonic sensing platform. In: Proceedings of 2011 7th International Symposium on Advanced Topics in Electrical Engineering, vol. 1, pp. 12–14.
Ferreiro-Vila, E., González-Díaz, J., Fermento, R., González, M., García-Martín, A., García-Martín, J., Cebollada, A., Armelles, G., Meneses-Rodríguez, D., Sandoval, E., 2009. Phys. Rev. B 80, 125132. http://dx.doi.org/10.1103/PhysRevB.80.125132.
Ferreiro-Vila, E., Iglesias, M., Paz, E., Palomares, F.J., Cebollada, F., González, J.M., Armelles, A., García-Martín, J.M., Cebollada, A., 2011. Phys. Rev. B 83, 205120. http://dx.doi.org/10.1103/PhysRevB.83.205120.
Fontana, E., Pantell, R., 1988. Phys. Rev. B 37, 3164–3181.
Ghatak, A., 2010. Optics. The McGraw-Hill Companies Inc., New York.
González-Díaz, J., García-Martín, A., Armelles, G., García-Martín, J., Clavero, C., Cebollada, R., Lukaszew, R., Skuza, J., Kumah, D., Clarke, R., 2007. Phys. Rev. B 76, 153402. http://dx.doi.org/10.1103/PhysRevB.76.153402.
Goodman, P., 2002. Gold Bull. 35, 21–26.
He, P., McGahan, W., 1991. J. Appl. Phys. 69, 4021–4028.
Hu, J., Sun, X., Agarwal, A., Kimerling, L., 2009. J. Opt. Soc. Am. B 26, 1032–1041.
Johnsson, B., Löfås, S., Lindquist, G., 1991. Anal. Biochem. 198, 268–277. http://dx.doi.org/10.1016/0003-2697(91)90424-R.
Kahn D., 1992. Magnetic Properties and Structure of Cobalt Hardened Gold. SUR/FIN '92, vol. 1, pp. 305–341.
Karlsson, R., Katsamba, P.S., Nordin, H., Pol, E., Myszka, D.G., 2006. Anal. Biochem. 349, 136–147. http://dx.doi.org/10.1016/j.ab.2005.09.034.
Kockar, H., Meydan, T., 2002. Eur. Phys. J. B—Condens. 20, 435–438.
Kolomenski, A., Kolomenskii, A., Noel, J., Peng, S., Schuessler, H., 2009. Appl. Opt. 48, 5683–5691.
Le, K.Q., Bienstman, P., 2011. IEEE Photonics J. 3, 538–545. http://dx.doi.org/10.1109/JPHOT.2011.2156778.
Liu, H., Wang, B., Leong, E., Yang, P., Zong, Y., 2010. ACS Nano 4, 3139–3146.
Lofas, S., 1995. Pure Appl. Chem. 67, 829–834.
Ma, Y., Farrell, G., Semenova, Y., 2014. Photonics Nanostruct.—Fundam. Appl. 12, 69–74.
Manera, M.G., Ferreiro-vila, E., Cebollada, A., Miguel, J., Garc, A., Giancane, G., Valli, L., Rella, R., 2012. J. Phys. Chem. C 1, 10734–10742.
Manera, M.G., Montagna, G., Ferreiro-Vila, E., González-García, L., Sánchez-Valencia, J.R., González-Elipe, A.R., Cebollada, A., Garcia-Martin, J.M., Garcia-Martin, A., Armelles, G., Rella, R., 2011. J. Mater. Chem. 21, 16049. http://dx.doi.org/10.1039/c1jm11937k.
Mattox, D., 2010. Handbook of Physical Vapor Deposition (PVD) Processing, Second ed. Elsevier Inc., Boston.
Neuert, G., Kufer, S., Benoit, M., Gaub, H.E., 2005. Rev. Sci. Instrum. 76, 054303. http://dx.doi.org/10.1063/1.1899503.
Okamoto, H., Massalski, T., Nishizawa, T., Hasebe, M., 1985. Bull. Alloy Phase Diagr. 6, 449–454.
Okinaka, Y., 1998. Gold Bull. 31, 3–13.
Olaru, A., Gheorghiu, M., David, S., Wohland, T., Gheorghiu, E., 2009. J. Phys. Chem. B 113, 14369–14380.
Pištora, J., Lesňák, M., Vlašín, O., Cada, M., 2010. Opt. Appl. XL (4), 883–895.
Polyanskiy, M.N., 2014. Refractive Index Database. http://refractiveindex.info.
Raether, H., 1988. Surface plasmons on smooth and rough surfaces and on gratings.
Regatos, D., Fariña, D., Calle, A., Cebollada, A., Sepúlveda, B., Armelles, G., Lechuga, L. M., 2010. J. Appl. Phys. 108, 054502. http://dx.doi.org/10.1063/1.3475711.
Regatos, D., Sepúlveda, B., Fariña, D., Carrascosa, L.G., Lechuga, L.M., 2011. Opt. Express 19, 8336–8346.
Schasfoort, R., Tudos, A., 2008. Handbook of Surface Plasmon Resonance. The Royal Society of Chemistry, Cambridge.
Sepúlveda, B., Calle, A., Lechuga, L.M., Armelles, G., 2006. Opt. Lett. 31, 1085–1087.
Temnov, V.V., Armelles, G., Woggon, U., Guzatov, D., Cebollada, A., Garcia-Martin, A., Garcia-Martin, J.-M., Thomay, T., Leitenstorfer, A., Bratschitsch, R., 2010. Nat. Photonics 4, 107–111. http://dx.doi.org/10.1038/nphoton.2009.265.
Yang, K., Clavero, C., Skuza, J., 2010. J. Appl. Phys. 107, 103924.
Zhan, S., Wang, X., Liu, Y., 2011. Meas. Sci. Technol. 22, 025201. http://dx.doi.org/10.1088/0957-0233/22/2/025201.
Zvezdin, A., Kotov, V., 1997. Modern Magnetooptics and Magnetooptical Materials. IOP Publishing Ltd., Bristol, Philadelphia.